Pore Network Modeling of Fibrous Gas Diffusion Layers for Polymer Electrolyte Membrane Fuel Cells

Jeff T. Gostick, Marios A. Ioannidis, Michael W. Fowler*, Mark D. Pritzker

Department of Chemical Engineering
University of Waterloo, Waterloo, Ontario, Canada N2L 3G1

* Corresponding Author: mfowler@uwaterloo.ca

Keywords: polymer electrolyte membrane, fuel cell, gas diffusion layer, pore network modeling, mass transfer, permeability, diffusivity, capillary pressure.

Abstract

A pore network model of the gas diffusion layer (GDL) in a polymer electrolyte membrane fuel cell is developed and validated. The model idealizes the GDL as a regular cubic network of pore bodies and pore throats following respective size distributions. Geometric parameters of the pore network model are calibrated with respect to porosimetry and gas permeability measurements for two common GDL materials and the model is subsequently used to compute the pore-scale distribution of water and gas under drainage conditions using an invasion percolation algorithm. From this information, the relative permeability of water and gas and the effective gas diffusivity are computed as functions of water saturation using resistor-network theory. Comparison of the model predictions with those obtained from constitutive relationships commonly used in current PEMFC models indicates that the latter may significantly overestimate the gas phase transport properties. Alternative relationships are suggested that better match the pore network model results. The pore network model is also used to calculate the limiting current in a PEMFC under operating conditions for which transport through the GDL dominates mass transfer resistance. The results suggest that a dry GDL does not limit the performance of a PEMFC, but it may become a significant source of concentration polarization as the GDL becomes increasingly saturated with water.

1. Introduction

Polymer electrolyte membrane fuel cells (PEMFCs) are a promising energy conversion technology. However, there are still several technological difficulties that must be overcome before they can be commercialized. One of the main challenges is to achieve effective water management inside the cell, since the presence of water can be both detrimental and beneficial to PEMFC performance and durability. A highly humidified environment is preferred in the cell to maintain membrane hydration and conductivity. Excess humidity, however, results in condensation and blockage of pores in the electrode backing or gas diffusion layer (GDL). These effects are complicated by the fact that water is a product of the oxygen reduction reaction in the cathode compartment. At high current densities, the increased rate of water production can lead to liquid water formation and flooding of the GDL. An additional difficulty is that the environmental conditions inside the cell, such as temperature, pressure and gas compositions, can vary widely over the active area of a cell [1,2]. As a result, ideal humidity conditions may exist in one location while liquid water may form elsewhere. Clearly, understanding of the formation, behavior and movement of liquid water inside the porous components of the PEMFC is of great importance.

A large number of multiphase flow models have recently appeared in the literature that attempt to address the problem of liquid water behavior in the cathode and its impact on mass transfer in a PEMFC [3-10]. The models presented to date are exclusively based on continuum descriptions of flow and transport, which require knowledge of constitutive relationships. These include the dependences on water saturation of the relative permeability, effective diffusivity and air-water capillary pressure. At present, GDL-specific experimental data on gas or liquid phase relative permeability are scarce, the effective diffusivity has been estimated only from numerical models [11] and only recently have air-water capillary pressure data been made available [12]. As a result, many of the necessary relationships and parameters incorporated in elaborate multiphase transport models remain uncertain and application of these models to different GDL materials is questionable.

An alternative approach to modeling multiphase transport processes in GDL materials is pore network modeling. This approach has a long history in the study of porous media of geologic origin (soil and rock) [13-16]. The basis of this approach is a mapping of a complex pore space continuum onto a regular or irregular lattice of sites and bonds. To derive a geometrical model it is usually assumed that the pore space can be conceptually partitioned into a collection of pore bodies communicating through local constrictions termed pore throats. Model pore networks are thus constructed by assigning pore and throat sizes to the lattice sites and bonds, respectively. Simplifying assumptions regarding the shape of pores and throats are invariably made to facilitate the computation of capillary and transport characteristics of the pore network elements [17]. Pore network models are ideally suited for the simulation of low-capillary number (quasi-static) immiscible displacement using percolation concepts [13]. A main advantage of pore network models is that they account explicitly for pore-level physics and pore space geometry/topology. Prediction of various macroscopic transport and capillary properties of porous media is relatively straightforward if the geometric, topological and correlation properties of the porous microstructure are properly specified. The task of extracting this information is, however, non-trivial, typically requiring extensive characterization of 3D volume data [18].

The present work outlines the development of a pore network model to study multiphase transport in GDLs. This is the first attempt to deploy pore network modeling for the study of the gas diffusion layer of a PEMFC, although Thompson [19] has applied a pore network modeling approach to conventional paper. Numerous modifications are made to the traditional pore network modeling framework in order to account for the unique geometric aspects of fibrous GDLs. In the absence of 3D volume data for the GDL materials studied, the network parameters are obtained by calibration to experimental gas permeability and drainage capillary pressure data. The model is then used to simulate multiphase transport scenarios of interest to PEMFC operation, such as the diffusion of gas through a partially water-filled GDL and the convective flow of gas and water under conditions of partial water saturation. Results are presented for two typical GDL materials for which the necessary experimental information is available. Finally, calculations of limiting current densities are performed by placing typical fuel cell boundary conditions on the network model and calculating the mass transfer flux through partially saturated GDLs to the catalyst layer.

2. Model Development

2.1. Materials to be Modeled

In this work, the porous networks of two different types of carbon paper are modeled. Fig. 1 shows micrographs of SGL Sigracet® 10BA and Toray 090. Toray 090 has a mostly 2D structure with linear fibers arranged in layers in the plane of the paper. SGL 10BA has a more 3D structure with intertwined, curved fibers. Physical properties of each material are listed in Table 1.

2.2. Pore Network Construction

One of the distinguishing features of GDLs is that they possess a very high porosity, which can range from 0.75 to above 0.90, meaning that GDLs are predominantly void space. Moreover, there is little constriction between pores, creating a highly open structure. Fig. 2 shows a cross-sectional slice obtained from a simple solid model of a GDL. With such small solid phase fraction, it is difficult to define distinct pore bodies or to identify pore throats. This situation is quite different from the one encountered in rocks and soils, for which pore bodies and pore throats can be intuitively delineated in images of the pore space.

2.2.1. Pore and Throat Size Distributions

The pore network model developed here for GDLs is based on the one described by Ioannidis and Chatzis [17] and Chang and Ioannidis [20]. The pores are modeled as nodes on a regular cubic lattice, interconnected with throats. The pores are idealized as cubic bodies and the throats are treated as ducts of square cross-section. This arrangement is shown in Fig. 3 with the relevant dimensions labeled. The use of square pores is convenient in order to achieve sufficiently high porosities and to qualitatively describe the presence of corners and crevices in the pore space. The pore network is constructed by assigning pore body sizes from a truncated Weibull cumulative distribution:

$$b_{p,i} = \lambda \left[-ln\left(1 - \chi \cdot \chi_{max}\right)\right]^{-1/\kappa} + b_{min} \tag{1}$$

where $b_{\mathrm{p,i}}$ is the radius of the i^{th} pore, χ is a random number between 0 and 1, χ_{max} (< 1) scales the random number and truncates the upper end of the distribution to prevent excessively large pores from being generated, b_{min} is the minimum pore radius and λ and κ are adjustable parameters that control the location/spread and shape of the distribution. A Weibull distribution is used since it is highly versatile and mathematically simple [17], containing only two adjustable parameters. These features are advantageous when pore size distribution is adjusted to calibrate the model as described in Section 3.1.

Once pore sizes are assigned, throat sizes are assigned by assuming that the size of each throat is equal to the size of the smallest of the two adjacent pores. This throat assignment scheme is chosen because it allows for minimum constriction between pore bodies, creating a highly open structure characteristic of GDLs. Fig. 4a shows the construction of the lattice with pores and throats identified. Fig. 4b shows only the void and solid space of the same lattice. The open nature of the pore space obtained by this method of throat size assignment is apparent.

The length of each throat is calculated as the difference between the lattice constant L_C and the size of the two connecting pores. The lattice constant is the spacing between pore centers and is adjusted to match the porosity of the network model to the known porosity of the material. This is discussed further in Section 3.2. Consequences of this size assignment scheme are that throats and pores have similar size and their volume cannot be neglected in the calculation of the total lattice volume. In fact, a throat is actually an extension of the pore body to which it is attached and the lattice is basically an assembly of pores connected directly to pores.

It should be clear that the aforementioned description is by no means an attempt to reproduce the actual geometry of GDL pore space. What is sought instead is to endow the pore network model with sufficient flexibility to reproduce experimental measurements of capillary pressure and gas permeability (in-plane and through-plane). Obviously, a better way to construct the pore network would be to extract its geometric and topological properties from experimental 3D volume data of the GDL materials.

2.2.2. Spatial Correlation of Pores Sizes

One of the key features included in the model is spatial correlation of pore sizes. A highly porous material such as a GDL contains regions of extended continuous void space with no solid to mark distinct boundaries between pore bodies. In terms of the pore network model, these regions are analogous to multiple neighboring pores of similar size. Imposing spatial correlation of pore sizes in the model results in pores of similar size being placed next to each other in the lattice. These pores are invaded by the non-wetting phase at similar capillary pressures and offer similar resistance to fluid flow, therefore acting as a single, large pore. The effect of introducing spatial correlation of pores into the model is to increase the permeability of the network by more than 20% and bring it more in line with measured values. Experience has shown that without spatial correlation, it is very difficult to match both the experimental permeability and the capillary pressure curves, since both are dependent on pore size distribution (see further discussion in Section 3).

Spatial correlation also partially accounts for the observed directional anisotropy in the permeability tensor [21]. When pores are correlated in certain directions, the permeability along these directions is increased. It was found that correlating pores in the direction of fiber alignment helped to create the observed anisotropy trends. For instance, since the fibers of Toray 090 are aligned in the *x*-*y* plane, correlation of neighboring pores in this plane, but not in the through-plane (*z*-direction), produces the correct trend. This is summarized with the notation [β_x,

β_y, β_z] = [1, 1, 0] where β is the correlation distance. The fibers in SGL 10BA are also predominantly aligned in the *x*-*y* plane, but have additional directional alignment in the *x*-direction. The use of correlation distances [β_x, β_y, β_z] = [2, 1, 0] partially reproduces the observed anisotropy. Fig. 5a shows a structure obtained using a field of random, uncorrelated numbers, whereas Fig. 5b and Fig. 5c show the structures obtained when the correlations [1, 1, 0] and [2, 1, 0], respectively, are imposed.

Anisotropy can also be created in the model by constricting throat sizes along specific directions. In addition to the imposition of spatial correlation, a small amount of throat constriction was necessary to completely match the experimentally observed anisotropy in permeability. Throats were uniformly constricted according to the expression:

$$b_{t,ij} = \alpha\, b_{p,i} \tag{2}$$

where $b_{t,ij}$ is the size of the throat connecting pores i and j, $b_{p,i}$ is the size of pore i with $b_{p,i} < b_{p,j}$ and α is the throat constriction factor. The throat constriction factor is direction dependent and described with the notation [α_x, α_y, α_z]. In general it was necessary to constrict throats slightly (5-10%) in the direction perpendicular to the axis of fiber alignment. For Toray 090 throats were constricted in the through-plane z-direction according to [α_x, α_y, α_z] = [1, 1, 0.9]. In SGL 10BA, the fibers are aligned in the *x*-*y* plane with some additional alignment in the *x*-direction. Accordingly, throat constriction factors [α_x, α_y, α_z] = [1, 0.95, 0.95] were used. Constricting throats in this way is consistent with the structure of GDLs since flow in the cross-fiber direction is more obstructed.

2.3. Capillary Pressure

All pore throats and pore bodies in this model are assumed to be of square cross-section. The capillary pressure, P_C, required for a non-wetting fluid to penetrate a throat of square cross-section is estimated by the Young-Laplace equation:

$$P_C = -2\gamma \cos\theta \left(\frac{1}{b_t} \right) \tag{3}$$

where γ is the surface tension, θ is the contact angle and b_t is the radius of the largest circle that can be inscribed in the square capillary. Contact angles in GDL materials are not easily determined. The contact angle on simple carbon is highly variable [22]. In a previous study [12], an experimental procedure was described for estimating the microscopic contact angle of mercury on GDL fibers by measuring the macroscopic contact angle of a sessile drop on the GDL surface and correcting for the porosity and roughness of the surface. It was estimated that the microscopic mercury contact angle could be as low as 110°. In the present work, an angle of 115° was used. We measured macroscopic contact angles of water on the two GDLs of this study and adopted the same procedure to estimate their corresponding microscopic contact angles. Table 2 lists the values so obtained. We note that GDL materials containing carbon and

Teflon are expected to have non-uniform wettability, although no data are presently available to quantify this expectation. The pore network detailed here can be modified to accommodate non-uniform contact angles.

2.4. Late Pore Filling

In reality, pore geometry is more complex than any simple geometric shape, albeit angular, can describe. Unresolved length scales due to the presence of cracks, corners, crevices and interstitial regions at fiber-fiber contact points amount to pore space from which the wetting phase is displaced at capillary pressures higher than corresponding to first entry of the non-wetting phase into any pore in the network. To account for the gradual drainage of the wetting phase from such small scale features, we employ the following expression [20]:

$$s_{wp} = s_{wp}^{*}\left(\frac{P_C^{*}}{P_C}\right)^{\eta} \quad ,P_C > P_C^{*} \tag{4}$$

where η is the filling exponent, s_{wp} is the wetting phase saturation of a given pore at capillary pressure P_{C}, and s_{wp}^{*} is the wetting phase saturation of the same pore at the capillary pressure, P_C^{*}, corresponding to first entry (breakthrough) of the non-wetting phase. The parameters η and s_{wp}^{*} are adjustable. Late pore filling enables smaller scale features to affect the capillary pressure behavior of the network without explicitly including them as individual pores. This treatment was found to be necessary to correctly model the experimental capillary pressure curves.

2.5. Drainage Simulation

The process considered by the present model is the drainage of a wetting phase by slow (quasi-static) invasion of a non-wetting phase. In terms of fuel cell operation, this simulation corresponds to the flow of liquid water (the non-wetting phase) from the catalyst layer through the GDL to the flow channel, via a path of the largest accessible pores. The algorithm for simulating drainage in the network is as follows. First, an initial, low capillary pressure is selected. The network is then scanned and all pore throats that *could* be penetrated at that given capillary pressure are marked as ‘open’, along with the pore bodies to which they are connected. Next, all distinct clusters of contiguous open throats and pores are found and labeled. Finally, all clusters that are connected to the injection face are identified and are counted as invaded by the invading fluid. All pores and throats not connected to the injection face are returned to a ‘closed’ state. In this way, the invading front of the non-wetting phase only reaches pores that are both topologically accessible from the injection face (i.e. through other invaded pores) and penetrable at the given capillary pressure. The algorithm proceeds by increasing the capillary pressure in small increments and repeating the procedure until all pores and throats are open or filled with the invading fluid. The volume of non-wetting phase within pores that are invaded at each capillary pressure step is calculated and a capillary pressure curve is generated. In the present simulations, the injection of the non-wetting phase is always in the through-plane (*z*) direction. In terms of a GDL, the injection face is on one side of the paper and the exit face is the other side.

2.6. Transport Processes in the Network

2.6.1. Convection

Determination of the flow rate and pressure drop across the pore network requires solution of the following mass conservation equation over each pore:

$$q_i = \sum_{j=1}^{n} g_{ij}\left(P_j - P_i\right) = 0 \tag{5}$$

where i denotes the current pore, j denotes the neighboring pore, n is the number of neighbors, q_i is the net flow through pore i, g_{ij} is the hydraulic conductivity for flow between pore i and the neighboring pore j, while P_i and P_j are the pressures in each pore. The hydraulic conductivity, g_h, of the pores and throats depend on their size and length and is determined from the following expression for square ducts [23]:

$$g_h = \frac{2.28b^4}{2L\mu} \tag{6}$$

where $2b$ is the size of the conduit opening, μ is the fluid viscosity and L is the conduit length. L is equal to b for pore bodies and calculated for pore throats as discussed in Section 2.2. The total hydraulic conductivity for flow between two adjacent bodies is taken as the net conductivity for flow through half of pore i, the connecting throat and half of pore j. The hydraulic conductivity, g_h, for each section is calculated using Eq.(6) and the net conductivity for the pore-throat-pore assembly, as shown in Fig. 3, is found from linear resistor theory for resistors in series:

$$\frac{1}{g_{h,ij}} = \frac{1}{g_{h,pi}} + \frac{1}{g_{h,t}} + \frac{1}{g_{h,pj}} \tag{7}$$

Eq.(5) is set up for each pore in the network to yield a system of linear equations that can be solved in conjunction with the prescribed boundary pressures on each side of the network to give the total flow (Q) across the network [17]. Once Q is known, the permeability of the network can be found from Darcy's law:

$$Q = \frac{KA}{\mu l}\left(P_{in} - P_{out}\right) \tag{8}$$

where K is the absolute permeability, P_{in} and P_{out} are arbitrarily chosen inlet and outlet boundary pressures. For flow in the Z direction, $A = X \cdot Y \cdot L_C^2$ is the area of pore network normal to the direction of flow and $l = Z \cdot L_C$ is the length of the pore network in the direction of flow. X, Y and Z are the dimensions of the network in number of pores and L_C is the lattice constant, discussed in more detail in Section 3.2.

2.6.2. Diffusion

The diffusivity of the network is found in the same manner as for fluid flow. Fick's law for binary diffusion of A through stagnant B is:

$$N_A = -\frac{cD_{AB}}{1-x_A}\frac{dx_A}{dl} = \frac{cD_{AB}}{x_B}\frac{dx_B}{dl} = cD_{AB}\frac{d\ln x_B}{dl} \tag{9}$$

where D_{AB} is the binary diffusion coefficient, c is the mole concentration, x_A is the mole fraction of species A, x_B is the mole fraction of species B ($x_B = 1 - x_A$), and l is the length of the domain. Using Eq.(9), the species conservation equation at each network node is then written:

$$n_i = \sum_{j=1}^{n} g_{d,ij}\left(ln\, x_{B,j} - ln\, x_{B,i}\right) = 0 \tag{10}$$

where n_i is the mass transfer rate through pore i, $x_{B,j}$ is the concentration in the neighboring pore j, and $x_{B,i}$ is the concentration in pore i. g_d is analogous to the hydraulic conductivity and is calculated for a given conduit as:

$$g_d = \frac{cD_{AB}(2b)^2}{L} \tag{11}$$

where D_{AB} is the diffusion coefficient and $2b$ is the width of the conduit. The conductivity for diffusion through each half pore and throat is calculated using Eq.(11) and the net conductivity for the entire conduit is found from:

$$\frac{1}{g_{d,ij}} = \frac{1}{g_{d,pi}} + \frac{1}{g_{d,t}} + \frac{1}{g_{d,pj}} \tag{12}$$

Upon solution of the system of species conservation equations, the effective diffusivity of the network is found using Fick's law:

$$N_A \approx \frac{cD_{eff}A}{l}\left(\ln x_{B,in} - \ln x_{B,out}\right) \tag{13}$$

where D_{eff} is the effective diffusivity of the network. $x_{\text{B,in}}$ and $x_{\text{B,out}}$ are the inlet and outlet mole fractions of the stagnant species B.

2.6.3. Multiphase Transport

In order to study conditions relevant to PEMFC operation, it is necessary to model the transport of gas and liquid as a function of water saturation in the GDL. This can be done by calculating the water and gas effective permeability and the gas diffusivity after the network has been partially invaded by the non-wetting phase (water), over a range of saturations. The general approach is to modify the conductivity of individual pores and throats as they become invaded by the non-wetting fluid and to recalculate the overall transport through the network. Since a certain amount of wetting phase is always present within pores and throats invaded by the non-wetting phase, due to late pore filling effects, careful attention must be paid to this modification, particularly in view of the fact that the precise geometry and connectivity of the remaining wetting phase is unknown. Two limiting cases are considered:

Case 1 – Once a pore is penetrated with the invading fluid (water), the residual wetting phase is no longer conductive. This case represents the most pessimistic scenario for gas transport since it leads to a highly obstructed and disconnected network with increasing invading fluid saturation.

Case 2 – The residual wetting phase within pores and throats invaded by the non-wetting phase maintains a connection with neighboring pores and offers limited conductivity to mass transfer through films and corners, which is modeled by assuming that the area for mass transport varies directly with the volume fraction of the conducting phase in a given pore. This case represents the most optimistic scenario for gas transport since it neglects the tortuosity of the pore space containing the residual wetting phase.

In general, for both cases the expressions for hydraulic and diffusive conductivity (Eqs.(6) and (11)) become:

$$g_{h,i} = \frac{2.28 b_i^4}{2L\mu}\left(s_{\sigma p}\right)^m \tag{14}$$

and:

$$g_{d,i} = \frac{cD\left(2b_i\right)^2}{L}\left(s_{\sigma p}\right)^n \tag{15}$$

where $s_{\sigma\mathrm{p}}$ is the volume fraction of conducting phase in pore i. The exponents m and n control the behavior of the pore saturation correction and depend on the conducting phase and case of interest. For Case 1, m = 2 and n = 1 for the non-wetting phase, while m and n are both equal to infinity for the wetting phase. The latter situation sets the conductivity to 0 for all pores that are invaded ($s_{\mathrm{wp}} < 1$). For Case 2, $m = 2$ and $n = 1$ for both phases.

3. Model Calibration

3.1. Pore and Throat Size Distribution

The first step in the calibration of a pore network model is to identify the pore size distribution that enables the model to match experimentally determined drainage capillary pressure data. The computed drainage capillary pressure curves for SGL 10BA and Toray 090 were compared to previously reported MIP data [12] for the displacement of air by mercury. Fig. 6 shows a comparison of the experimental data and the model curves obtained, while Fig. 7 shows histograms of pore size and throat size distributions used to generate these curves. The parameters for the Weibull distribution (Eq.(1)) obtained by fitting are listed in

Fluid	Surface Tension	Contact Angle[1]	
		SGL 10BA	Toray 090
Mercury	0.480 $N \cdot m^{-1}$	115°	115°
Water	0.072 $N \cdot m^{-1}$	100°	98°
Octane	0.022 $N \cdot m^{-1}$	0°	0°

Table 3. The mean number averaged pore diameters for Toray 090 and SGL 10BA obtained from these fit distributions are 19 μm and 33 μm, respectively. These values agree well with the results of Tomadakis and Robertson [24], who calculated pore size distributions and mean pore sizes for solid models of various fiber arrangements and porosities. They also agree with similar data obtained recently by Schulz et al. [25] for simulated Toray 090 and SGL 10BA materials. The fit in the high capillary pressure region obtained for the SGL 10BA sample was ignored since the pore space in this region represents sub-pore scale roughness of the PTFE coating and binder materials (visible in Fig. 1b,ii). The computed capillary pressure curves both rise more sharply than the experimental ones due to the use of a rather narrow pore size distribution, which is necessary to match the high porosity (see Section 3.2).

To further assess the validity of the capillary pressure curves generated by the model, simulations were run with octane as the wetting fluid and air as the invading fluid. This corresponds to experiments performed using the method of standard porosimetry [12]. The advantage of considering this system is that octane is a highly wetting fluid and its contact angle can be confidently taken equal to 0°. It should be noted that the Weibull distribution parameters listed in

Fluid	Surface Tension	Contact Angle[1]	
		SGL 10BA	Toray 090
Mercury	$0.480\ \mathrm{N \cdot m^{-1}}$	115°	115°
Water	$0.072\ \mathrm{N \cdot m^{-1}}$	100°	98°
Octane	$0.022\ \mathrm{N \cdot m^{-1}}$	0°	0°

Table 3 and obtained above by fitting the model to the MIP data were also used for the octane-air system. The only parameters that differ were the surface tension and contact angle of octane (see Table 2). The good agreement between the simulated and experimental capillary pressure curves also shown in Fig. 6 supports the validity of the pore and throat size distributions selected. It is possible, however, that other pore and throat size distributions than those given in

Fluid	Surface Tension	Contact Angle[1]	
		SGL 10BA	Toray 090
Mercury	0.480 N·m^{-1}	115°	115°
Water	0.072 N·m^{-1}	100°	98°
Octane	0.022 N·m^{-1}	0°	0°

Table 3 could also lead to a match between the computed and measured capillary pressure curves. It is necessary to compare model predictions to other experimental results, such as absolute permeability and porosity, to improve confidence in the characterization of the two GDL materials in terms of the distributions given in

Fluid	Surface Tension	Contact Angle[1]	
		SGL 10BA	Toray 090
Mercury	0.480 N·m^{-1}	115°	115°
Water	0.072 N·m^{-1}	100°	98°
Octane	0.022 N·m^{-1}	0°	0°

Table 3.

3.2. Lattice Constant

The lattice constant is the distance between pore centers in the cubic lattice. For a given set of pore sizes, adjusting the lattice constant controls the porosity of the network. For instance, if the lattice constant is large, then a significant amount of distance will exist between pores, thereby increasing the solid fraction and reducing the porosity. In the present work, the lattice constant was determined in the following manner. First, a pore size distribution was selected. Then an initial guess was made for the lattice constant and corresponding throat volumes (i.e. lengths) determined. This also allowed the porosity (ε) of the network for a fixed total void volume to be calculated from:

$$\varepsilon = \frac{V_P + V_t}{L_C^3 \cdot X \cdot Y \cdot Z} \tag{16}$$

where V_p is the total pore volume of the network, V_t is the total throat volume, X, Y and Z are the dimensions of the network expressed in terms of the number of pores and L_C is the lattice constant. The value of L_C was adjusted until the calculated porosity matched the experimental value for the material. Finally, it was verified that L_C was larger than the largest pore in the network to ensure that no pores overlapped. If this criterion was not met, then the pore size distribution was adjusted and the process repeated.

Preventing the overlap of pores is necessary to avoid several inconsistencies in the network geometry, such as pore volumes being counted twice, throat lengths being negative and the center-to-center distance between pores being larger than L_C. Also, if pores were allowed to overlap, it would be trivial to match porosity, since any pore size distribution would suffice. Allowing such flexibility in the pore size distribution would also enable a near-perfect matching of the capillary pressure curve since an arbitrarily broad distribution could be used. On the contrary, requiring that no pores overlap tightly constrains the range of pore size distributions that can be used. For instance, if the pore size distribution is very wide, the network contains many small pores. Since the lattice constant is on the order of the largest pore, these small pores are surrounded by a substantial amount of solid, making it impossible to have a sufficiently high porosity. In the present work, it was necessary to use a pore size distribution that gave a slightly steeper capillary pressure curve than the experimental data (Fig. 6) in order to match the porosity. The ability to match the porosity, while still achieving a good agreement of the capillary pressure curves, is a strong indicator of the appropriateness of the pore size distributions for such high porosity materials.

The value of L_C obtained also indicates the appropriateness of the model geometry since L_C has units of length and represents the spacing between pore centers. The lattice constant for Toray 090 has a value of 25.2 μm and indicates that 11 pores on average span the thickness of the material. SGL 10BA has a lattice constant of 40.5 μm, corresponding to 10 pores across its thickness. These values are consistent with information on their structures obtained from SEM images of GDL cross-sections [12].

3.3. Absolute Permeability

The final aspect of the model calibration is to compare the permeability of the network with measured permeability values. Comparing the model results to permeability data allows for verification of pore information that is not reflected in the capillary pressure curve, such as pore lengths and connectivity. It has been experimentally observed [21] that the in-plane permeability is higher than the through-plane permeability, a result that has been verified numerically [26] and analytically [27]. As discussed in Section 2.2.2, spatial correlation of pore sizes is included in the network in combination with slight throat constrictions in order to reproduce the observed anisotropy in the model. Measurements on Toray 090 indicate that the in-plane permeability is about 1.5 – 2 times higher than that in the through-plane direction (Table 1). As discussed in Section 2.2.2, spatial correlation distances of [β_x, β_y, β_z] = [1, 1, 0] and throat constriction factors of [α_x, α_y, α_z] = [1, 1, 0.9] have been used in order to fully match the permeability data. This procedure reproduces the anisotropy and gives good agreement between experimental data and model results, as can be seen in

	Toray 090	SGL 10BA
Network Size Parameters		
L_C	25.2 μm	40.5 μm

Pore Size Distribution Parameters		
λ	5.25	9
κ	3	3.5
b_{min}	5 μm	9 μm
χ_{max}	0.95	0.9
Late Pore Filling Parameters		
s^*	0.20	0.20
η	1.00	1.00
Throat Constriction Factors		
$[\alpha_x, \alpha_y, \alpha_z]$	[1, 1, 0.9]	[1, 0.95, 0.95]
Pore Correlation Distances		
$[\beta_x, \beta_y, \beta_z]$	[1, 1, 0]	[2, 1, 0]

Table 4. The anisotropy of SGL 10BA was somewhat more complicated due to the alignment of fibers, which caused the permeability to differ from one in-plane direction to the other. To capture this, correlation distances of $[\beta_x, \beta_y, \beta_z] = [2, 1, 0]$ are used along with throat constriction factors of $[\alpha_x, \alpha_y, \alpha_z] = [1, 0.95, 0.95]$.

4. Model Validation

4.1. Effective Diffusivity

Determination of the effective diffusivity of the network provides a useful means of independently verifying the chosen network geometry. Although experimental data for diffusion through GDLs are not yet available, limited numerical results have been presented by Tomadakis and Sotirichos [28] for fibrous materials with various arrangements of fiber alignment that correspond to GDL materials. The effective diffusivities predicted by the present model are compared with those of Tomadakis and Sotirichos [28] in Table 4. The agreement is reasonable considering that no efforts were made to fit the model to those values.

	Toray 090	SGL 10BA
Network Size Parameters		
L_C	25.2 μm	40.5 μm
Pore Size Distribution Parameters		
λ	5.25	9
κ	3	3.5
b_{min}	5 μm	9 μm
χ_{max}	0.95	0.9
Late Pore Filling Parameters		
s^*	0.20	0.20
η	1.00	1.00
Throat Constriction Factors		
$[\alpha_x, \alpha_y, \alpha_z]$	[1, 1, 0.9]	[1, 0.95, 0.95]
Pore Correlation Distances		
$[\beta_x, \beta_y, \beta_z]$	[1, 1, 0]	[2, 1, 0]

4.2. Liquid Water Injection

Recent experiments have been performed by Benziger et al. [29] to measure the breakthrough pressure of liquid water in GDLs. In these experiments, the static pressure of a column of liquid water above a GDL is increased until liquid penetrates the sample. The pressure required for water breakthrough on various samples has been reported, including a sample of Toray 120 with no PTFE treatment. This material is thicker than the Toray 090 considered here, but otherwise similar in structure. An experimental value of 3300 Pa was found, which compares with a value of 2483 Pa predicted by the present model. These values are within 25% of each other, which is reasonable considering that the materials are not necessarily identical. The reasonable agreement between the model and data suggest that the contact angle used for water on Toray 090 is reasonably correct. Similar data are not available for SGL 10BA.

5. Results and Discussion

5.1. Relative Permeability

In the presence of two or more phases, the permeability of each phase P is reduced since the number of available pathways is reduced by the presence of the other phase(s). This effect is expressed in terms of relative permeability $K_{r,P}$ defined as the ratio of the effective phase permeability $K_{eff,P}(s_P)$ in the presence of another phase to the absolute permeability, or single phase, permeability K, i.e.,

$$K_{eff,P}(s_P) = K \cdot K_{r,P}(s_P) \tag{17}$$

where s_P is the volume fraction of phase P in the network. $K_{r,P}$ depends on the magnitude of saturation and history of saturation change (drainage or imbibition) and varies between 0 and 1. In studies employing continuum models the functional form of $K_{r,P}$ has been assumed to be:

$$K_{r,P} = s_p^a \tag{18}$$

where a is typically taken as 3 in the fuel cell modeling literature [30]. Equation (18) is one of several empirical models of relative permeability and, to the best of our knowledge its applicability to two-phase flow in fuel cell materials lacks experimental support.

Relative permeability calculations using the pore network model are based on the assumption that the pore-scale fluid occupancy is dictated exclusively by capillary forces – an assumption appropriate for low capillary number displacements. To examine the effect of GDL anisotropy, the effective permeability was calculated in the x, y *and* z directions through the network to yield the results plotted in Fig. 8. Non-wetting fluid invasion was always in the through-plane direction, which corresponds to liquid water flow from the catalyst layer through the GDL to the flow channels. Also shown in Fig. 8 for comparison are the curves obtained using Eq.(18) with a = 3 for the two GDL materials. These results have been normalized for the intrinsic anisotropy of each material and so the directional differences observed reflect the anisotropic effects caused by the presence of liquid water. This saturation-dependent anisotropy is due to the preferential spreading of the invading phase in the direction of highest permeability, which is the direction of largest and most easily invaded pores. One of the major consequences of water spreading preferentially in the plane of the material is the significant reduction of gas transport in the through-plane direction. This suggests that the ideal GDL is one where the typical anisotropy ratio is not only minimized, but reversed. Higher through-plane permeability would simultaneously limit detrimental liquid water spreading and increase the intrinsic transport rates to the catalyst layer. A broad analysis of the effects of anisotropy in the GDL is given by Pharaoh et al. [31].

An important feature of these results is the non-zero liquid water saturation required for liquid water to break through the GDL. For Toray 090, the simulations show that liquid water saturations of 20% are necessary before a continuous liquid path spans the full thickness of the GDL. For SGL 10BA, the necessary liquid saturation is 10%. Below this critical liquid saturation, the liquid water permeability through the GDL is zero. This behavior is not described by the general form of the relative permeability function in Eq.(18) which predicts finite water permeability at vanishing water saturations. Nonetheless, the results obtained using Eq.(18) (i.e. the dashed line) are in rough agreement with pore network calculations of water relative permeability in the through-plane direction.

Predictions of the relative gas phase permeabilities are also shown in Fig. 8. The gas phase permeability was calculated for both cases discussed in Section 2.6.3. In Case 1, the residual gas in an invaded pore offers no conductivity and gas flows entirely through the network of connected gas-filled pores. In Case 2, gas is allowed to flow through the non-filled portion of invaded pores. Both of these cases are somewhat unrealistic, for Case 1 prevents any flow through the space occupied by gas within water-invaded pores whereas Case 2 allocates to this space the hydraulic conductance of a straight conduit of reduced size. These cases, therefore, provide lower and upper bounds of gas permeability, respectively. The Case 1 results show that no gas conductivity exists above a critical water saturation of 65% for Toray 090 and 70% for SGL 10BA. A significant amount of gas still exists in the network at this critical saturation, but it is completely surrounded or trapped by the invading phase and is hydraulically disconnected from either the gas inlet or outlet face. Case 2 does not show a critical water saturation, since all trapped gas pores maintain some hydraulic conductivity. This case matches the behavior of Eq.(18) very closely. Since Case 2 unrealistically allows gas transport to occur unimpeded through the corners of pores that are mostly filled with water, then Eq.(18) must be also be considered a limiting case. Eq.(18) requires a to be about 5 to match the model results for Case 1.

Cases 1 and 2 exhibit other differences due to anisotropy as liquid water saturation is increased. Case 1 shows significantly reduced permeability in the through-plane direction due to spreading of liquid water in the x-y direction, whereas Case 2 shows little to no anisotropy caused by additional liquid water. The latter effect arises because gas can leak through a pore even if it is mostly filled with water and allow pockets of trapped gas phase to contribute to mass transfer, thus minimizing the impact of in-plane liquid spreading.

5.2. Dependence of Effective Diffusivity on Water Saturation

The diffusion of gas from the flow channels to the catalyst layer is the predominant mode of reactant transport in a conventional PEMFC. As with gas convection, the presence of liquid water in the porous medium greatly reduces gas diffusivity. The reduction of the diffusion coefficient due to the presence of liquid water is given as follows:

$$D_{eff}(\varepsilon, s_w) = D_{AB} \cdot D_{rP}(s_w) \cdot f(\varepsilon) \tag{19}$$

where $D_{eff}(\varepsilon, s_w)$ is the effective diffusion coefficient, D_{AB} is the bulk diffusion coefficient, $D_{rP}(s_w)$ is the relative diffusivity and $f(\varepsilon)$ accounts for the reduction of diffusivity due to porosity and tortuosity. In fuel cell modeling literature, the Bruggeman approach is almost invariably adopted, leading to $f(\varepsilon) = \varepsilon^{1.5}$, although other estimates are available (see [32] and references therein), including one specifically for fibrous media [26]. Eq.(19) is analogous to Eq.(17). The function $D_{rP}(s_w)$, which is here called relative effective diffusivity due to its analogy to the relative permeability, has not been as widely studied, particularly for GDL materials. Nam and Kaviany [11] have performed a numerical study using a rudimentary network model. The pore network studied by these authors lacked a pore size distribution and could not be tailored to specific GDL materials. More importantly, in the model of Nam and Kaviany [11] water saturation was established with no regard for the physics of immiscible displacement. They suggested that the relative effective diffusivity decreases with the square of water saturation:

$$D_{rP}(s_P) = s_P^a \tag{20}$$

where a = 2. Values of a = 1.5 are also commonly used [3] based on the assumption that the Bruggeman correlation for the effect of porosity also applies to the effect of liquid water saturation.

The present model was used to calculate relative effective diffusivity in a GDL using invasion percolation concepts that more realistically simulate the configuration of water expected in an operating fuel cell. Specifically, liquid water was injected into the network in the through-plane direction to simulate liquid water flowing from the catalyst layer to the gas channels. The present model also includes pore and throat size distributions that adequately reproduce both the absolute permeability and effective diffusivity through a dry network. The results are shown in Fig. 9 along with those using Eq.(20) with $a = 2$.

The difference between Case 1 and Case 2 is much more dramatic for gas diffusivity than for gas permeability. This is due to the fact that diffusional conductivity is proportional to the area available for transport, while hydraulic conductivity is proportional to the square of the area. Since the area for transport through a pore is assumed to be proportional to the volume fraction of a pore that is filled with gas, the diffusional conductivity is much less hindered by the partial filling of pores. The large discrepancy between these two limiting cases underscores the need for experimental data concerning these transport processes. An argument against Case 2 is that not only does it fail to display a critical water saturation (above which effective gas diffusivity is zero), but it predicts significant diffusivity at near full-water saturation ($D_{rG}(s_w = 0.9) = 0.1$), which appears unrealistic. Case 1 shows a significant decrease in diffusivity as water invades the network. Compared to Eq.(20), diffusivities predicted by Case 1 can be several times lower. An exponent of $a = 5$ would be necessary in

Eq.(20) to approximate the behavior of the network model in this case. Clearly, current models could be significantly overestimating the transport rates through partially saturated GDLs.

Also shown in Fig. 9 are the liquid phase diffusivities. These values are not of direct interest to PEMFC performance calculations since liquid phase diffusion of reactants through the GDL is not significant. However, an area of research that is becoming increasingly active is the transport of ionic contaminants (e.g. Fe(II)), in the liquid phase. Thus, the presented results provide an estimate of diffusivities to be used in modeling contaminant transport in PEMFCs.

5.3. Limiting Current

An effort was also made to use the present network model to predict the limiting current in an operating PEMFC assuming that the GDL is the sole source of mass transfer resistance. This was undertaken in order to determine if and when mass transfer resistance in the cathode GDL becomes a significant portion of the overall mass transfer resistance [33]. By estimating the maximum rate of oxygen mass transfer that can be expected through a partially saturated GDL the limiting current was calculated and compared with typically observed values in operating cells.

The modeled domain is shown in Fig.10. The size of the domain is equivalent to 1 mm × 1 mm × δ, where δ is the GDL thickness (Table 1). This corresponds to a domain size of 40 × 40 × 12 pores for Toray 090 and 26 × 26 × 10 pores for SGL 10BA. On the channel side of the domain, half of the inlet face is blocked to simulate the effect of 1 mm lands and channels. The conditions in the flow channel are taken as fully humidified air at 80°C and 10 kPa gauge. The catalyst layer is treated as a reactive interface where the oxygen concentration is zero (i.e. limiting current conditions). Since the cell is fully humidified there is no water vapor diffusion and all water generated by the electrochemical reaction is in the liquid state. As a result, the mass flux through the GDL is considered to be molecular diffusion of O_2 through a stagnant film of N_2 and H_2O. This allows the multicomponent diffusion problem to be reduced to a binary diffusion problem, provided that the diffusion coefficient is calculated with appropriate consideration for the composition of the stagnant gas mixture [34]. Once the mass flux through the GDL is known, the current density is found from Faraday's Law.

The predicted limiting currents for both GDLs and both wetting phase conductivity cases are given in Fig.11. The limiting currents through dry Toray 090 and dry SGL 10BA are very similar to each other. Although Toray 090 is 25% thinner than SGL 10B, it is less porous and has a lower intrinsic effective diffusivity. These two factors offset each other and neither GDL is clearly better in terms of mass transfer performance under dry conditions. As water is added to the GDLs, however, the performance of the two materials diverges; the limiting current for SGL 10BA drops more quickly. This can be attributed to the increased spreading of liquid water in the *x*-*y* plane of this material.

The overall behavior for both materials shows a dramatic decrease in limiting current as the GDL fills with water. At low water saturations (<10%), the predicted limiting current through the GDL is higher than in a typical fuel cell, which can be between 1 and 2 A/cm^2. This indicates that at relatively dry conditions, the GDL is not the main source of concentration polarization, and performance is limited by other factors (i.e. the catalyst layer or electrolyte phase). When the GDL becomes wet, however, there is a significant reduction in the limiting current due to mass transfer resistance in the GDL. Case 1 predicts that at water saturations above 25% the maximum current density is less than 1 A/cm^2, indicating that mass transfer resistance through the GDL could be a dominant factor limiting PEMFC performance. The limiting currents for Case 2 do not drop as sharply in the presence of water and 75% saturation must be reached before it reaches 1 A/cm^2.

At present, insufficient experimental evidence is available to fully understand the configuration and connectivity of the residual gas phase in GDL pores invaded by water. Some experimental evidence concerning the amount of liquid water in the GDL of an operating fuel cell does exist, however. Kramer et al. [35] used neutron imaging to measure the water content in the cathode GDL during fuel cell operation and found saturations between 25% and 35% at limiting currents between 0.6 and 1.0 A/cm^2, which corresponds very closely with the results of Case 1. Other neutron imaging studies suggest a limiting current above 1 A/cm^2

at somewhat higher water saturation (30% - 60%) [36,37], which lies between Case 1 and Case 2. Obviously, more conclusive evidence is needed to verify the present model, but the reasonable agreement with these experimental results does lend support to the applicability of the network modeling approach.

6. Conclusions

A pore network model was developed to help understand the multiphase flow properties of GDL materials and estimate their multiphase flow and transport properties. A detailed description of the model was provided, with particular emphasis on integrating into the model both qualitative and quantitative aspects of the microstructure of high-porosity fibrous GDLs. The model was calibrated to two commonly used GDL materials by adjusting the model parameters to match available experimental results, specifically the absolute permeability tensor and drainage capillary pressure curves. Material-specific relative gas and liquid permeabilities and diffusivities were computed as functions of water saturation under conditions of quasi-static drainage of air by water and transport rates through the pore network were determined. Uncertainty regarding the configuration of the residual wetting phase (gas) in water-invaded pores of the material made it necessary to consider two limiting cases for gas transport: Case 1 in which residual gas phase is not conductive, and Case 2 in which the conductivity of the pore space occupied by gas in water-invaded pores is optimal. The results of these simulations were compared with commonly used models of relative permeability and diffusivity. It was found that these models tended to agree with Case 2, which likely overestimates mass transfer in the gas phase. Alternative forms of these common models were proposed that match the pore network modeling results of Case 1. This study further highlights an urgent need for experimental measurement of the effects of water saturation on water relative permeability and gas diffusivity.

Limiting current calculations were performed by implementing PEMFC boundary conditions and physical parameters on the network model. The limiting current was estimated at various water saturation levels for a GDL section in which one-half was open to the gas channel and the other half was covered by a land. A dry GDL can support limiting currents of nearly 4 A/cm^2, much more than is typically observed in operating fuel cells. When liquid water is present in the GDL, however, the predicted limiting current decreases rapidly to values typically observed in operating PEMFCs, indicating that mass transfer through the GDL may indeed be rate limiting at high current densities when the GDL is saturated with water.

7. Acknowledgements

The authors wish to thank the Natural Science and Engineering Research Council of Canada (NSERC) for financial support during the course of this study.

8. Nomenclature

Symbol	Description	Units
A	Area of lattice normal to flow direction	m^2
a	Exponent in Eq.(18) and Eq.(20)	
α	Throat constriction factor	
b	Conduit size (radius)	m
β	Spatial correlation distance	
c	Concentration	$mol \cdot m^{-3}$
χ	Random number in Weibull distribution	
D	Diffusion coefficient	$m^2 \cdot s^{-1}$
d_f	Fiber diameter	m
δ	GDL thickness	m
ε	Porosity	
g_h	Hydraulic conductivity	$m^3 \cdot Pa^{-1} \cdot s^{-1}$
γ	Surface tension	$N \cdot m^{-1}$
g_d	Diffusive conductivity	$m^3 \cdot s^{-1}$
η	Filling exponent	
K	Permeability	m^2
κ	Parameter in Weibull distribution	
L	Length of conduit	m
L_C	Lattice constant	m

L_t	Throat length	m
l	Length of pore network domain	m
λ	Parameter in Weibull distribution	
μ	Viscosity	Pa·s
N	Diffusion rate through network	$mol \cdot s^{-1}$
n	Diffusion rate through a pore conduit	$mol \cdot s^{-1}$
P_C	Capillary pressure	Pa
Q	Flow rate through network	$m^3 \cdot s^{-1}$
q	Flow rate through a pore conduit	$m^3 \cdot s^{-1}$
θ	Contact angle	radians
s	Saturation	
V	Volume	m^3
X	Lattice size in x-direction (in-plane)	No. of Pores
Y	Lattice size in y-direction (in-plane)	No. of Pores
Z	Lattice size in z-direction (through-plane)	No. of Pores

Subscripts

B	Species B
b	Bulk
CH	Gas channel
CL	Catalyst layer
eff	Effective
in	Inlet
nwp	Non-wetting phase

max	Maximum
out	Outlet
P	Phase
p	Pore
r	Relative
σ	Conducting phase
t	Throat
T	Total
w	Water
wp	Wetting phase
x	x direction (through-plane)
y	y direction (in-plane)
z	z direction (in-plane)

Superscripts

*	Value at pore breakthrough pressure
m	Exponent used in Eq.(14)
n	Exponent used in Eq.(15)

9. References

1. M. M. Mench, Q. L. Dong, and C. Y. Wang, In situ water distribution measurements in a polymer electrolyte fuel cell, J Power Sources 124 (2003) 90-98.
2. Q. Dong, J. Kull, and M. M. Mench, Real-time water distribution in a polymer electrolyte fuel cell, J Power Sources 139 (2005) 106-114.
3. U. Pasaogullari and C. Y. Wang, Two-phase modeling and flooding prediction of polymer electrolyte fuel cells, J Electrochem Soc 152 (2005) A380-A390.
4. A. A. Shah, G. S. Kim, W. Gervais, A. Young, K. Promislow, J. Li, and S. Ye, The effects of water and microstructure on the performance of polymer electrolyte fuel cells, J Power Sources 160 (2006) 1251-1268.
5. T. Berning and N. Djilali, A 3D, multiphase multicomponent model of the cathode and anode of a PEM fuel cell, J Electrochem Soc 150 (2003) A1589-A1598.
6. G. Lin, W. He, and T. V. Nguyen, Modeling liquid water effects in the gas diffusion and catalyst layers of the cathode of a PEM fuel cell, J Electrochem Soc 151 (2004) A1999-A2006.
7. A. Z. Weber, R. M. Darling, and J. Newman, Modeling two-phase behaviour in PEFCs, J Electrochem Soc 151 (2004) A1715-A1727.

8. N. P. Siegel, M. W. Ellis, D. J. Nelson, and M. R. Von Spakovsky, A two-dimensional computational model of a PEMFC with liquid water transport, J Power Sources 128 (2004) 173-184.

9. L. You and H. Liu, A two-phase flow and transport model for PEM fuel cells, J Power Sources 155 (2006) 219-230.

10. M. Acosta, C. Merten, G. Eigenberger, H. Class, R. Helmig, B. Thoben, and H. Muller-Steinhagen, Modeling non-isothermal two-phase multicomponent flow in the cathode of PEM fuel cells, J Power Sources 159 (2006) 1123-1141.

11. J. H. Nam and M. Kaviany, Effective diffusivity and water-saturation distribution in single- and two-layer PEMFC diffusion medium, Int J Heat Mass Trans 46 (2003) 4595-4611.

12. J. T. Gostick, M. W. Fowler, M. A. Ioannidis, M. D. Pritzker, Y. M. Volfkovich, and A. Sakars, Capillary pressure and hydrophilic porosity in gas diffusion layers for polymer electrolyte fuel cells, J Power Sources 156 (2006) 375-387.

13. F. A. L. Dullien, Porous Media: Fluid Transport and Pore Structure, Academic Press, New York, 1992.

14. M. Sahimi, Flow and Transport in Porous Media and Fractured Rock, VCH, Weinheim, 1995.

15. M. A. Celia, P. C. Reeves, and L. A. Ferrand, Recent adances in pore scale models for multiphase flow in porous media, Reviews of Geophysics 33 (1995) 1049-1057.

16. M. J. Blunt, M. D. Jackson, M. Piri, and P. H. Valvatne, Detailed physics, predictive capabilities and macroscopic consequences for pore-network models of multiphase flow, Adv Water Res 25 (2002) 1069-1089.

17. M. A. Ioannidis and I. Chatzis, Network modelling of pore structure and transport properties of porous media, Chem Eng Sci 48 (1993) 951-972.

18. Z. Liang, M. A. Ioannidis, and I. Chatzis, Geometric and topological analysis of three-dimensional porous media: Pore space partitioning based on morphological skeletonization, J Coll Interface Sci 221 (2000) 13-24.

19. K. E. Thompson, Pore-scale modeling of fluid transport in disordered fibrous materials, AICHE J 48 (2002) 1369-1389.

20. D. Chang and M. A. Ioannidis, Magnetization evolution in network models of porous rock under conditions of drainage and imbibition, J Coll Interface Sci 253 (2002) 159-170.

21. J. T. Gostick, M. W. Fowler, M. D. Pritzker, M. A. Ioannidis, and L. M. Behra, In-Plane and through-plane gas permeability of carbon fiber electrode backing layers, J Power Sources 162 (2006) 228-238.

22. A. Yan, X. Xiao, I. Kulaots, B. W. Sheldon, and R. H. Hurt, Controlling water contact angle on carbon surfaces from $5^{\text{o to 167o}}$, Carbon 44 (2006) 3116-3120.

23. R. Berker, "Integration des equation du mouvement d'un fluide visqueux incompressible," *Encyclopedia of Physics, VIII,* S. Flugge, ed., (Springer-Verlag, Berlin, 1963), 1-384.

24. M. M. Tomadakis and T. J. Robertson, Pore size distribution, survival probability, and relaxation time in random and ordered arrays of fibers, J Chem Phys 119 (2003) 1741-1749.

25. V. P. Schulz, J. Becker, A. Wiegmann, P. P. Mukherjee, and C. Y. Wang, Modeling of two-phase behavior in the gas diffusion media of PEFCs via full morphology approach, J Electrochem Soc 154 (2007) B419-B426.

26. M. M. Tomadakis and T. J. Robertson, Viscous permeability of random fiber structures: Comparison of electrical and diffusional estimates with experimental and analytical results, J Composite Materials 39 (2005) 163-188.

27. G. W. Jackson and D. F. James, Permeability of fibrous porous media, Can J Chem Eng 64 (1986) 364-374.

28. M. M. Tomadakis and S. V. Sotirchos, Transport properties of random arrays of freely overlapping cylinders with various orientation distributions, J Chem Phys 98 (1993) 616-626.

29. J. Benziger, J. Nehlsen, D. Blackwell, T. Brennan, and J. Itescu, Water flow in the gas diffusion layer of PEM fuel cells, J Membrane Sci 261 (2005) 98-106.

30. C. Y. Wang, Z. H. Wang, and Y. Pan, Two-phase transport in proton exchange membrane fuel cells, ASME HTD 364 (1999) 351-357.

31. J. G. Pharoah, K. Karan, and W. Sun, On effective transport coefficients in PEM fuel cell electrodes: Anisotropy of the porous transport layers, J Power Sources 161 (2006) 214-224.

32. J. van Brakel and P. M. Heertjes, Analysis of diffusion in macroporous media in terms of a porosity, a tortuosity and a constrictivity factor, Int J Heat Mass Trans 17 (1974) 1093-1103.

33. J. St-Pierre, B. Wetton, G. S. Kim, and K. Promislow, Limiting current operation of proton exchange membrane fuel cells, J Electrochem Soc 154 (2007) B186-B193.

34. C. R. Wilke, Diffusional properties of multicomponent gases, Chem Eng Prog 46 (1950) 95-104.

35. D. Kramer, J. Zhang, R. Shimoi, E. Lehmann, A. Wokaun, K. Shinohara, and G. G. Scherer, In situ diagnostic of two-phase flow phenomena in polymer electrolyte fuel cells by neutron imaging: Part A. Experimental, data treatment, and quantification, Electrochim Acta 50 (2005) 2603-2614.

36. A. Turhan, K. Heller, J. S. Brenizer, and M. M. Mench, Quantification of liquid water accumulation and distribution in a polymer electrolyte fuel cell using neutron imaging, J Power Sources In Press, Corrected Proof.

37. J. Zhang, D. Kramer, R. Shimoi, Y. Ono, E. Lehmann, A. Wokaun, K. Shinohara, and G. G. Scherer, In situ diagnostic of two-phase flow phenomena in polymer electrolyte fuel cells by neutron imaging: Part B. Material variations, Electrochim Acta 51 (2006) 2715-2727.

10. Figures

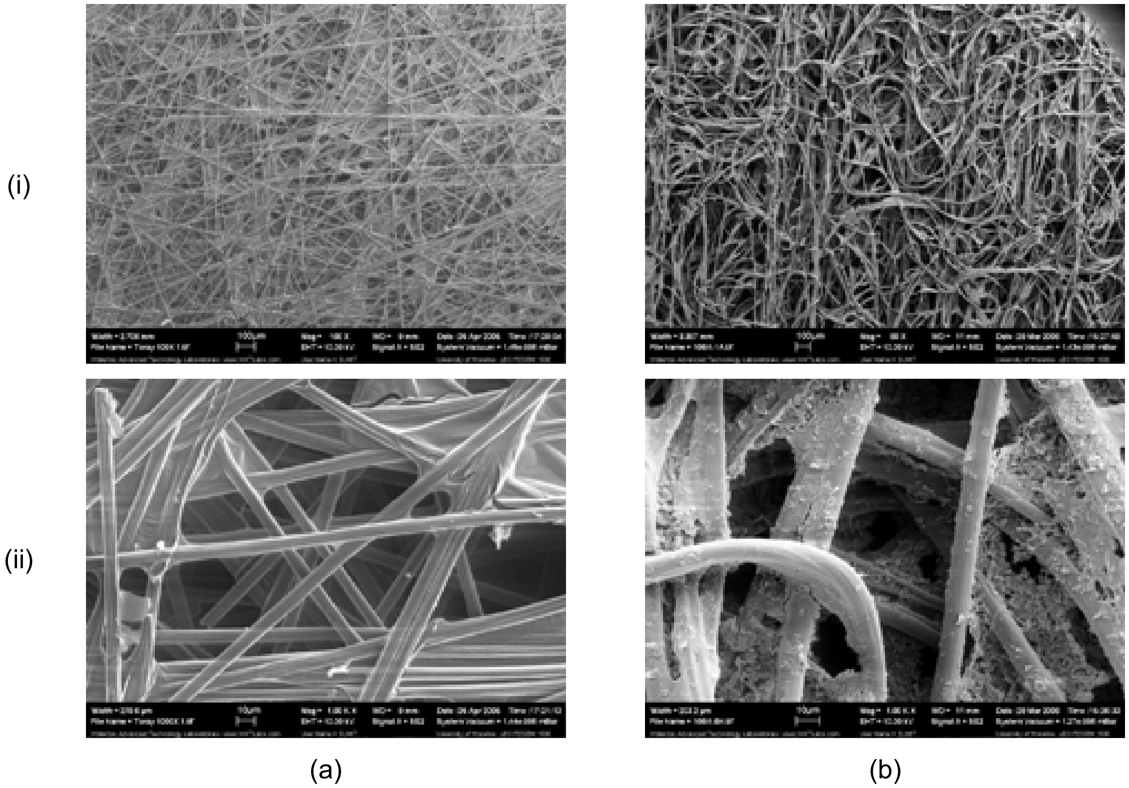

Fig. 1. SEM micrographs of GDL materials modeled in present study. (a) Toray 090, (b) SGL Sigracet 10BA. (i) 100x and (ii) 1000x magnification. The fiber alignment in the SGL10BA sample is apparent in (b)(i).

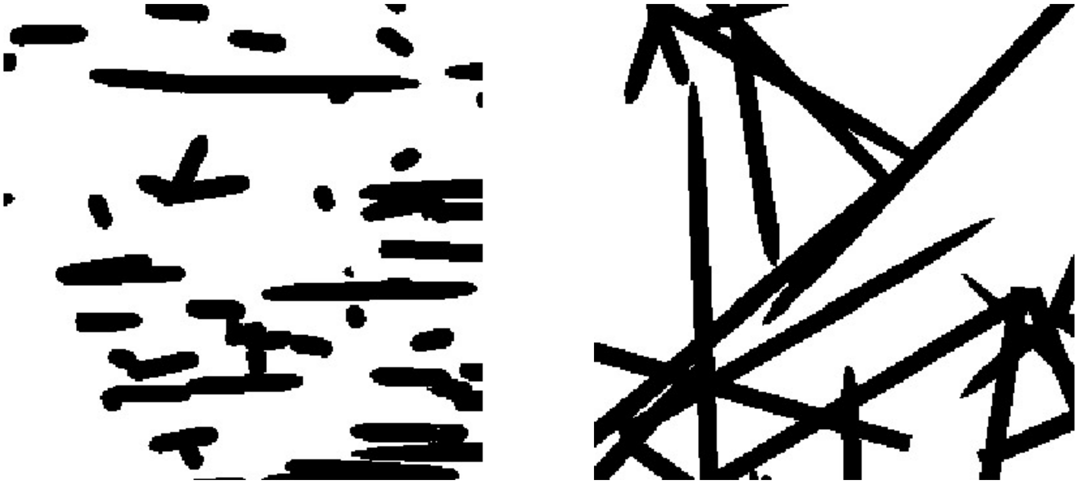

(a) (b)

Fig. 2. Slices of a simulated GDL solid model. (a) In-plane view, (b) through-plane view. Both views show 10 μm thick sections. The model was generated by placing fibers with a random location and in-plane rotation, then applying an out-of-plane rotation with angles normally distributed around 0° with a standard deviation = 1.

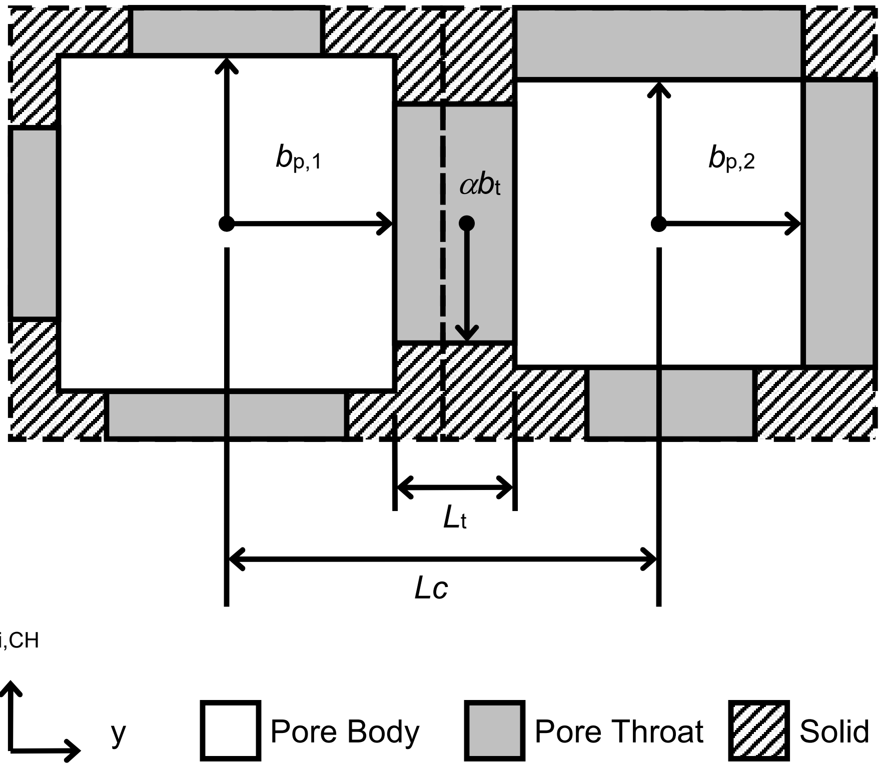

Fig. 3. Schematic of 2 neighboring pore bodies and connecting throat. Throat size (b_t) is proportional to the size of the smaller of the two connecting pores ($b_t = \alpha b_p$). Throat length (L_t) is equal to the difference between the pore body sizes (b_p) and the center-to-center distance between pores (L_C).

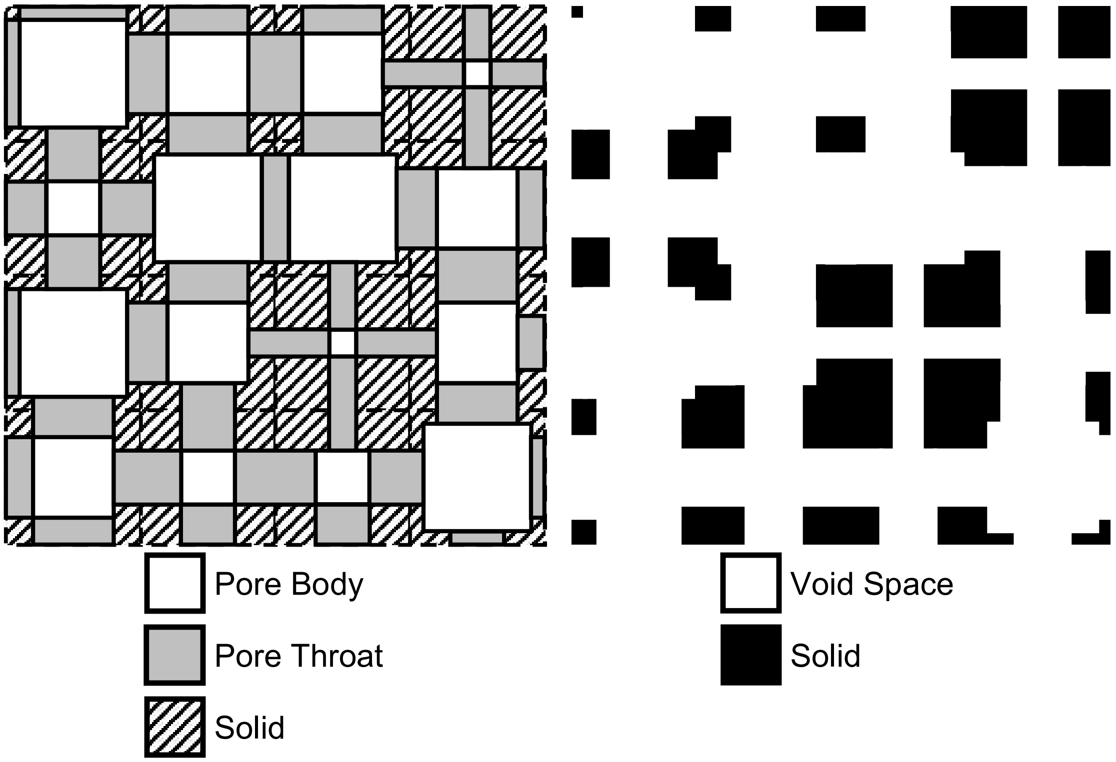

(a) (b)

Fig. 4. 2D Schematic of pore network construction. (a) Relationship between pores, throats and solid. (b) Structure in terms of void and solid space.

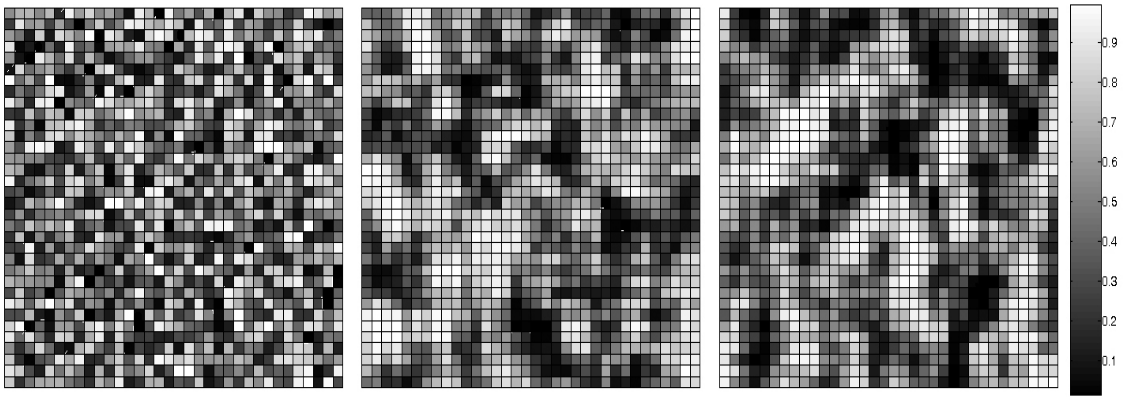

(a) (b) (c)

Fig. 5. Examples of spatially correlated random fields. (a) Uncorrelated field. (b) Correlated field used to model Toray 090 with correlation distances [1, 1. 0] in the *x*, *y* and *z* directions (z-direction not shown). (c) Correlated field used to model

SGL 10BA with correlation distances [2, 1, 0] in the *x*, *y* and *z* directions. (*z*-direction not shown).

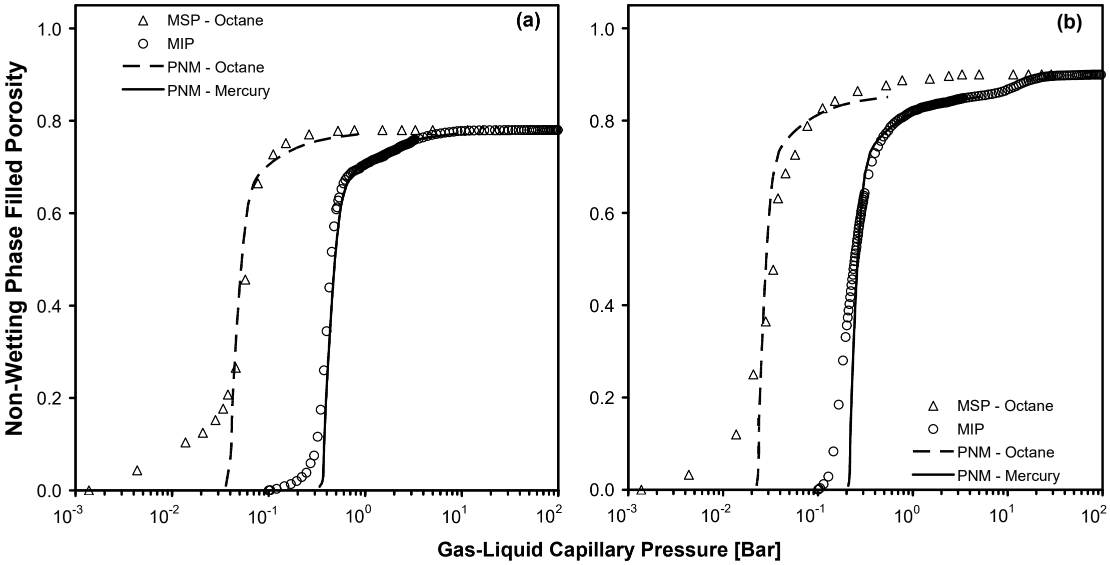

Fig. 6. Comparison of computed capillary pressure curves with experimental porosimetry data. (a) Toray 090 and (b) SGL 10BA. The high pressure feature in the SGL10BA (b) sample is attributable to the surface roughness visible in Fig. 1(b)(ii).

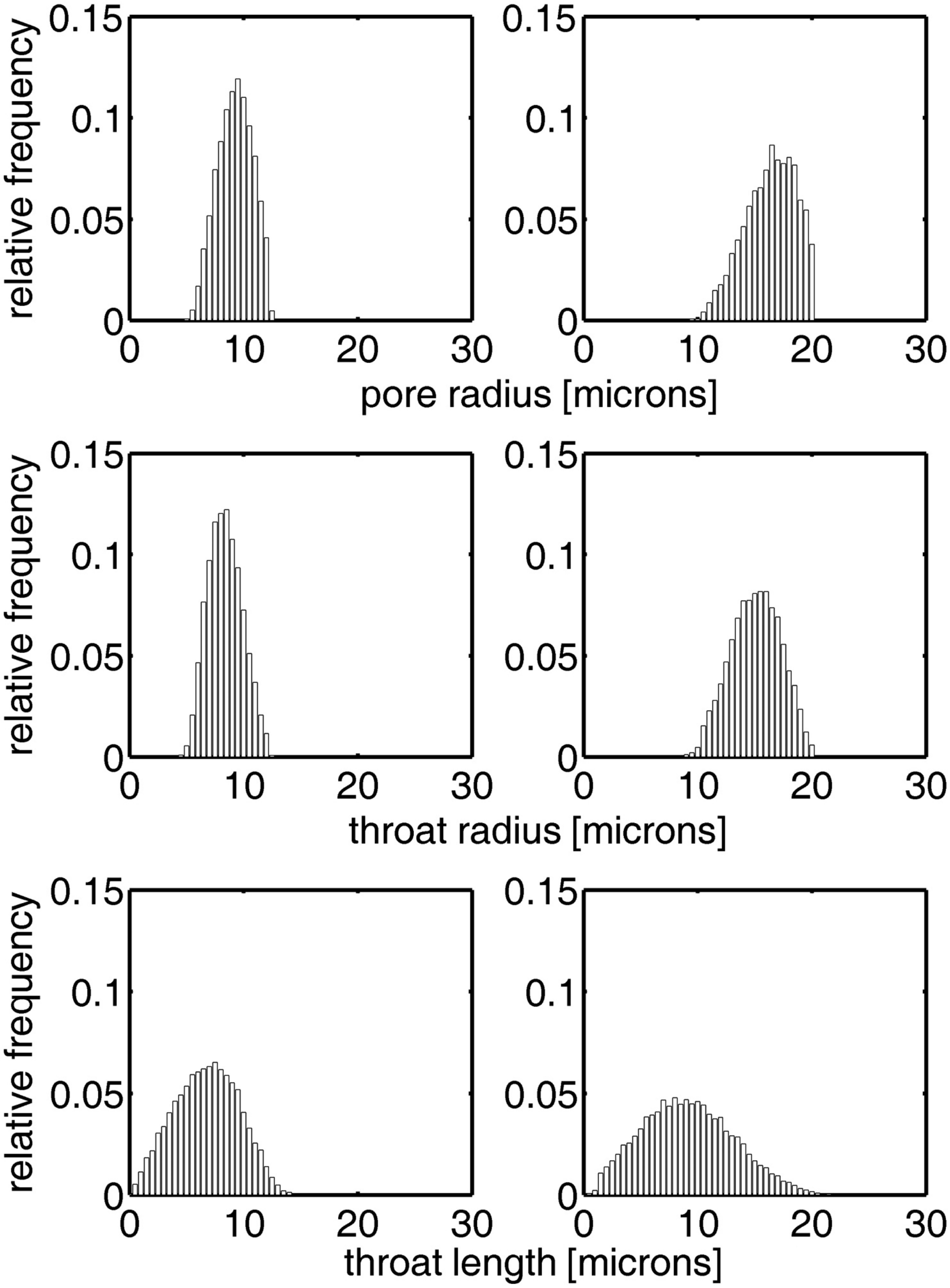

Fig. 7. Pore size, throat size and throat length histograms. (left) Toray 090 and (right) SGL10BA.

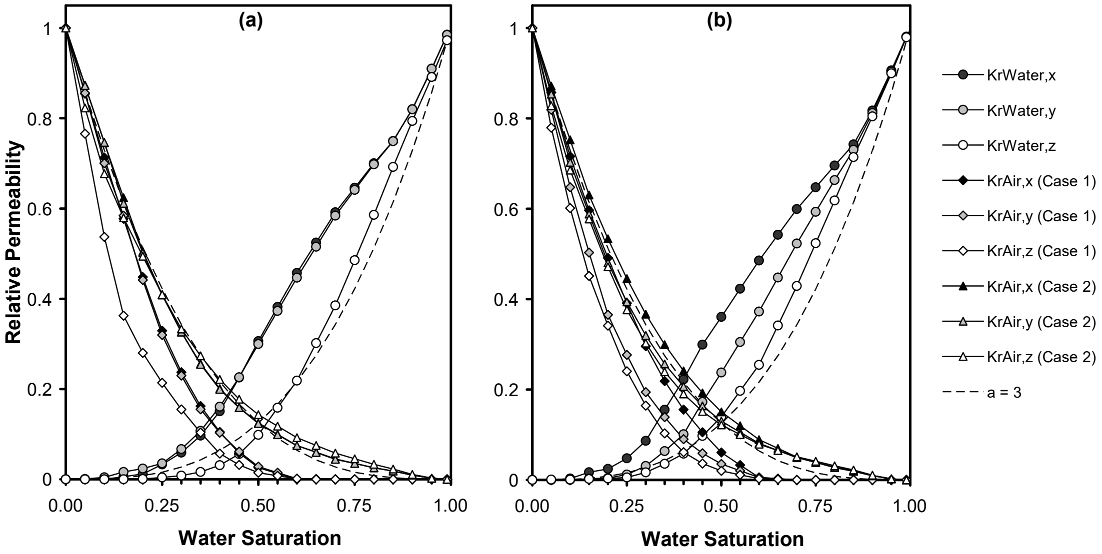

Fig. 8. Relative gas and liquid permeability as a function of water saturation in the network. (a) Toray 090 and (b) SGL 10BA. Both cases are shown for the gas relative permeability. Also shown is the result using Eq.(18) with exponent *a* = 3.

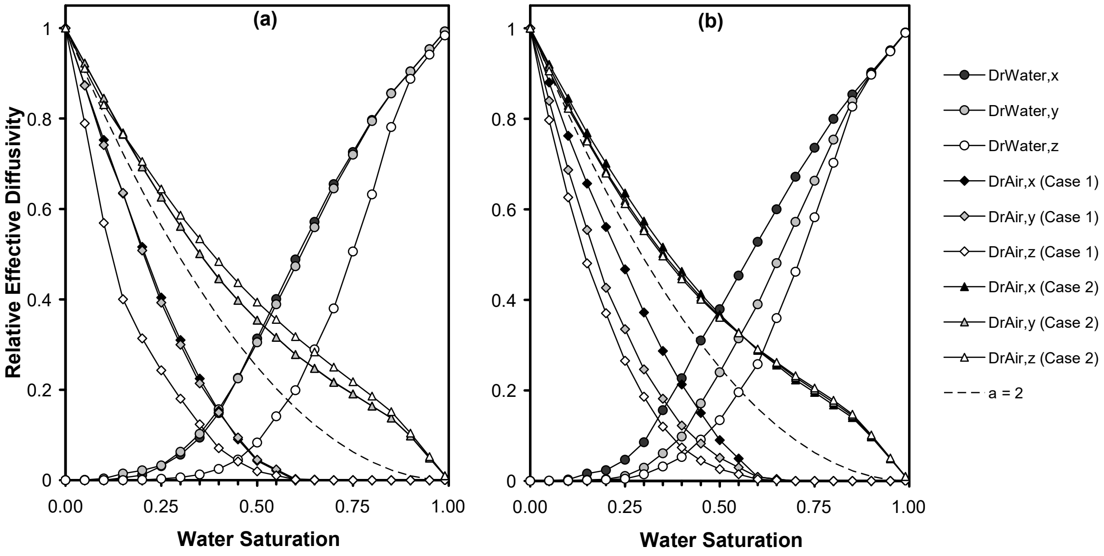

Fig. 9. Relative effective diffusivity as a function of water saturation in the network. (a) Toray 090 and (b) SGL 10BA. Both cases are shown for the

relative effective diffusivity of the air phase. Also shown is the result using Eq.(20) with exponent *a* = 2.

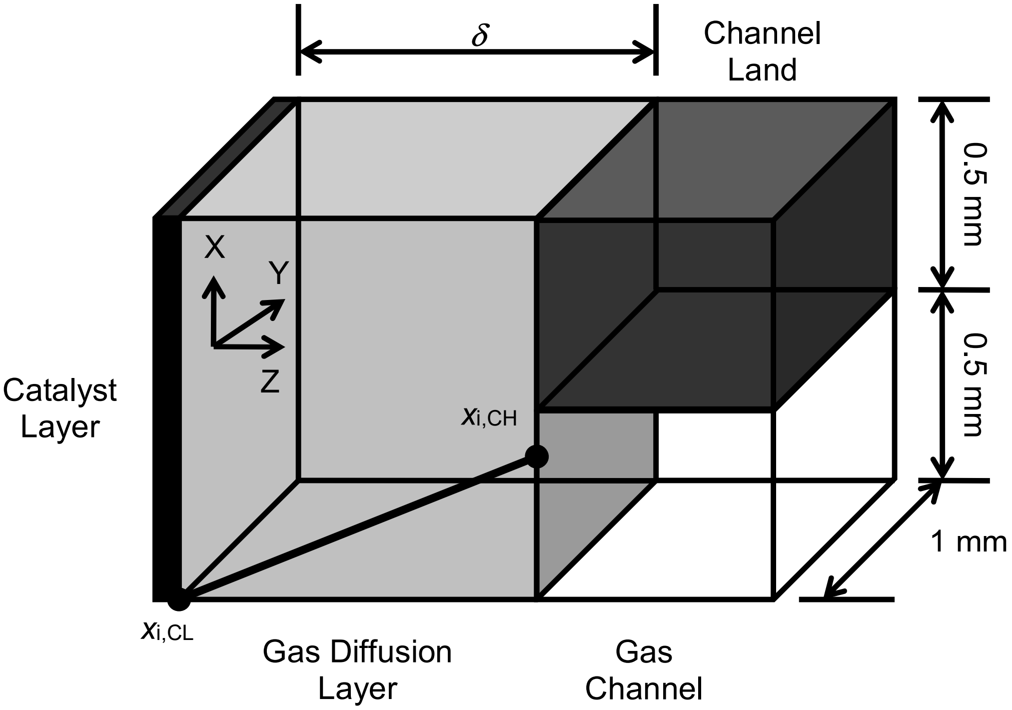

Fig.10. Schematic diagram of modeled domain. $x_{i,CH}$ is the concentration of species *i* in the flow channel, $x_{i,CL}$ is the concentration of species *i* at the catalyst layer.

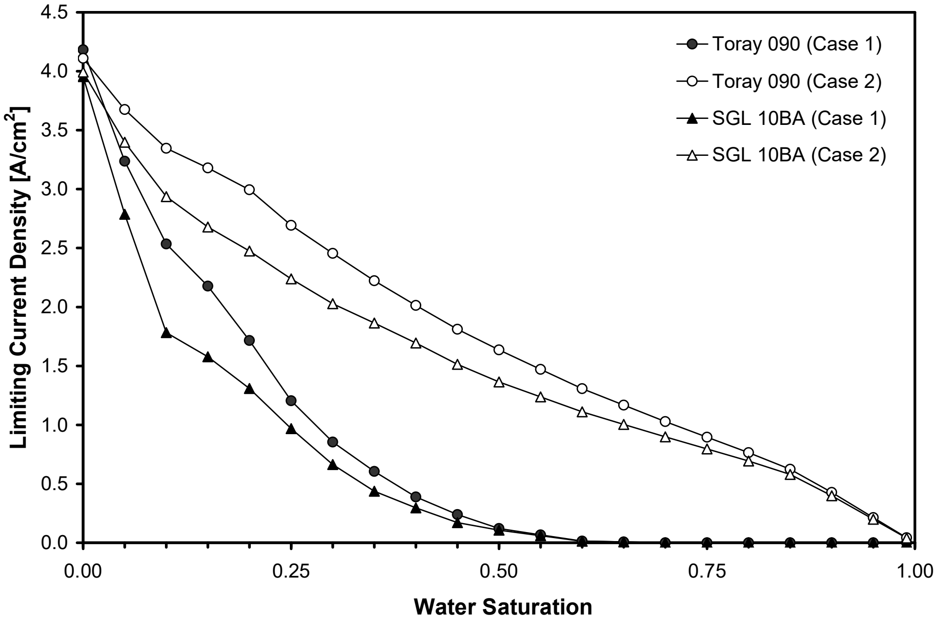

Fig.11. Predicted limiting current densities as a function of GDL water saturation based on mass transfer through the cathode GDL

11. Tables

Table 1. Physical Properties of GDL materials

Property	SGL 10BA	Toray 090
Thickness (δ)	390 μm	290 μm
Total Porosity (ε)	0.88-0.90	0.78-0.80
Fiber Diameter (d_f)	9 μm	9 μm
Permeability (K_x)	57×10^{-12} m^2	15×10^{-12} m^2
Permeability (K_y)	45×10^{-12} m^2	15×10^{-12} m^2
Permeability (K_z)	37×10^{-12} m^2	9.0×10^{-12} m^2

Table 2. Fluid properties

Fluid	Surface Tension	Contact Angle[1]	
		SGL 10BA	Toray 090
Mercury	0.480 N·m^{-1}	115°	115°
Water	0.072 N·m^{-1}	100°	98°
Octane	0.022 N·m^{-1}	0°	0°

Table 3. Model parameters used for each material

	Toray 090	SGL 10BA
Network Size Parameters		
L_C	25.2 μm	40.5 μm
Pore Size Distribution Parameters		
λ	5.25	9
κ	3	3.5
b_{min}	5 μm	9 μm
χ_{max}	0.95	0.9
Late Pore Filling Parameters		
s^*	0.20	0.20
η	1.00	1.00
Throat Constriction Factors		
$[\alpha_x, \alpha_y, \alpha_z]$	[1, 1, 0.9]	[1, 0.95, 0.95]
Pore Correlation Distances		
$[\beta_x, \beta_y, \beta_z]$	[1, 1, 0]	[2, 1, 0]

Table 4. Transport results for each modeled material

	Toray 090		SGL 10BA	
Permeability (x 10^{12} m^2)	Experimental [21]	Model	Experiment [21]	Model
K_x	15	14	57	54
K_y	15	14	45	48
K_z	9.0	9.5	37	39
Effective Diffusivity	Numerical [28]	Model	Numerical [28]	Model
$D_{e,x}$	0.67	0.54	0.78	0.64
$D_{e,y}$	0.67	0.54	0.75	0.61
$D_{e,z}$	0.62	0.46	0.75	0.58